

MOF-Assisted Nanocellulose Paper-Based Platform for Multiple Surface-Enhanced Raman Scattering Detection

Wenwen Yuan, Keran Jiao, Ruiqi Yong, Hang Yuan, Shan Cong, Fuzhou Niu,* Eng Gee Lim, Ivona Mitrović, Jinyu Zhou, and Pengfei Song*



Cite This: *Anal. Chem.* 2025, 97, 19136–19145



Read Online

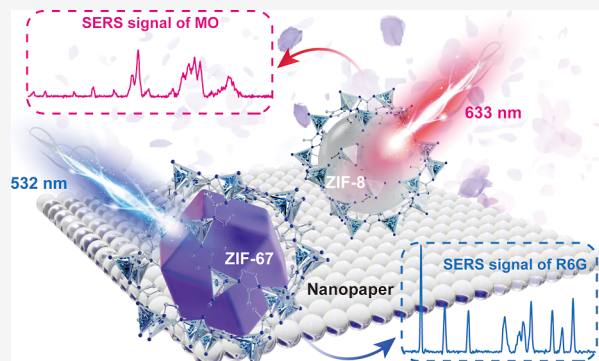
ACCESS |

Metrics & More

Article Recommendations

Supporting Information

ABSTRACT: Metal organic frameworks (MOFs), crystalline solids consisting of organic ligands and metal ions, have attracted increasing interest in various areas, including catalysis and biology. Functionalizable pore interiors and ultrahigh surface-to-volume ratios of MOFs make them excellent materials, especially for surface-enhanced Raman scattering (SERS) by the photoinduced charge transfer (PICT) between the MOFs and adsorbed molecules for SERS signal amplification. In our previous work, we demonstrated a p-n junction-assisted MOF substrate for enhancing the SERS signal through additional charge transfer, while the notable structural characteristics of MOFs benefit the SERS selectivity. However, due to this characteristic, a single MOF can only detect analytes at specific energy levels, thereby reducing the efficiency and limiting the detection range of SERS. To address this challenge, in this article, we attempted to synthesize multiple MOFs on the same substrate to achieve SERS with multiple detection functionality. In this study, we demonstrated a ZIF-8/Zn(OH)₂ n-n junction SERS substrate, which can achieve a 4.44 nM limit of detection using methyl orange (MO) as a model analyte, by trapping the additional electrons from Zn(OH)₂ to ZIF-8 to provide stronger electromagnetic enhancement. Then, we developed a multiple MOFs-based SERS analytical platform, incorporating both *in situ* ZIF-8 and ZIF-67, and utilized them together as SERS substrates. These two systems operated independently under different incident light wavelengths and successfully detected MO and Rhodamine 6G, respectively. Furthermore, this approach broadens the detection range of analytes while maintaining the tailorability and selectivity of MOF substrates simultaneously. This work offers a cutting-edge method for creating high-performance SERS substrates by demonstrating the ability to manipulate hot electrons for remarkable Raman amplification.



INTRODUCTION

Metal–organic frameworks (MOFs), a type of semiconductor material, are a desirable group of porous crystalline materials composed of metal centers coupled with organic ligands to produce well-organized frameworks.^{1,2} Catalysis, biology, and molecular separation are some of the most common applications for MOFs due to their high surface area, high porosity, structural tunability, and adequate chemical and thermal stabilities.^{2,3} Despite these applications, MOFs are also very attractive materials for surface-enhanced Raman spectroscopy (SERS). SERS, a powerful analytical method for molecular detection that can be achieved down to the single-molecule level, has been widely applied in catalysis chemistry,^{4,5} analyte analysis,^{6,7} and other areas.⁸ The scattering cross sections are increased by photoinduced charge transfer (PICT), which in turn amplifies the Raman signals between the semiconductor and adsorbed analytes.⁹ Compared with the conventional SERS substrates (noble metals), MOFs exhibit greater structural flexibility and higher specific surface areas.¹⁰ On one hand, the structural flexibility of MOFs

optimizes the charge transfer (CT) interactions between the probe molecules and the SERS substrates to boost the signals.¹¹ On the other hand, due to the extremely high specific surface areas of MOFs and their ability to modify their pore interiors, the detection limit may be further lowered, and the target molecules may be greatly enhanced.^{2,12}

MOFs have been extensively studied in SERS over the past decade, and several methods have been reported for the fabrication of highly selective MOF substrates.^{13,14} The first reported systematic research of MOF SERS substrates relies on acid treatment by Cong et al.¹³ They discovered that the presence of CT at the semiconductor–analyte contact area explains the MOFs exhibiting notable Raman enhancement.

Received: May 5, 2025

Revised: July 3, 2025

Accepted: July 24, 2025

Published: August 22, 2025



The limit of detection (LOD) was achieved as 10^{-8} M, which is insufficient for ultrasensitive detection. To reduce the LOD for satisfying real requirements, they have previously reported one method that introduced oxygen vacancy defects by increasing the photoexcitation of MOF materials.¹⁴ Nevertheless, the MOF SERS substrate's photoexcitation could not be used as a steady-state technique and remained stable for only 2 weeks. To address this problem, in our previous work we demonstrated a MOF/M_x(OH)_y (M_x(OH)_y-assisted, M = Co, Cu, and other metals) SERS substrate.¹⁵ We clarified the functioning of these p–n junction complexes, emphasizing the part excitons play in both conventional CT between MOF to analyte and effective PICT inside the p–n junction. The SERS LOD achieved was 10^{-10} M, surpassing 100× folds of the pure MOF substrate. Though these three methods provided a comprehensive exploration of MOF-based SERS detection, the detection range remained limited by the CT mechanism of MOFs, which only detects molecules at specific energy levels. In other words, MOFs can achieve SERS-specific detection within the energy levels that enable PICT under excitation energy; however, this also restricts the detection range of a single MOF substrate. To overcome this limitation, multi-component MOF substrates have been proposed for the detection of multiple molecules. Another strategy involves fabricating multicomponent materials by generating a MOF-supported noble metal SERS substrate. Although this method enables multiple detection, it cannot utilize the advantages of selectivity and flexibility of MOFs and only enhances the SERS signal through the original noble metals.¹⁶ Therefore, a MOF-based SERS substrate capable of multiple detection, without sacrificing the selectivity and sensitivity of the MOF substrate, urgently needs to be developed.

In this paper, we generated a ZIF-8/Zn(OH)₂ n–n junction nanostructure as a SERS substrate. ZIF-8 trapped electrons from Zn(OH)₂, and these electrons contributed to the enhancement, demonstrating the feasibility of using n–n heterojunctions of MOFs for SERS detection. As a proof of concept, the common Raman reporter methyl orange (MO) was employed as the model analyte, achieving a low LOD (4.44 nM) and a high enhancement factor (EF) of 3.07×10^5 . MOF materials can serve as a type of SERS substrate with molecular selectivity, which restricts the SERS detection for multiple analytes. To track this problem, we developed multiple MOFs-based SERS analytical devices (MOF-PADs) by generating both in situ ZIF-8 and ZIF-67 nanostructure on nanocellulose paper (nanopaper) plate. The features of nanopaper, such as its ultrasmooth surface, high optical transparency, and tunable chemical properties, make it a great platform for SERS detection.^{17,18} Furthermore, thanks to the abundant hydroxyl groups, metal ions can easily replace the hydrogen ions. This enables the facile generation of in situ MOF nanostructures using a straightforward ion layer absorption and reaction method, without a complex multilayer deposition on a traditional silicon substrate.¹⁹ Through shifting different incident light wavelengths to contribute PICT in independent systems, the sensitive detection of MO and Rhodamine 6G (R6G) was successfully realized on the MOF-PADs. The MOF-PADs can innovatively realize multiple SERS detection while retaining the selectivity of MOFs, without compromising sensitivity based on the CT mechanism. Our method provides a versatile platform for customized SERS detection, opening up an promising direction for further study and application.

EXPERIMENTAL SECTION

Materials and Reagents. (2,2,6,6-Tetramethylpiperidin-1-yl)oxyl (TEMPO)-oxidized nanofibrillated cellulose (NFC) slurry (1.0 wt % solid, carboxylate level 2.0 mmol/g solid, average nanofiber diameter: 10 nm) was purchased from Tianjin University of Science and Technology (Tianjin, China). R6G (AR), Na₂SO₄ (>99%), MO (>99%), and methanol (>99.5%) were obtained from Macklin (Shanghai, China). Co(NO₃)₂·6H₂O (>99%), Zn(NO₃)₂·6H₂O (>99%), NaOH (>97%), and 1,2-dimethylimidazole (>98%) were purchased from Aladdin (Shanghai, China). Ethanol (>99%) was ordered from Hushi (Shanghai, China).

Preparation of an In Situ ZIF-8 Nanoplate. We employed a coordination replication technique to establish a simple and scalable fabrication process for the in situ ZIF-8/Zn(OH)₂ n–n junction nanostructure on nanopaper (ZIF-8 nanoplate). The process involves five main steps, as shown in Figure 1: (i) 4.0 g of TEMPO-oxidized NFC slurry was

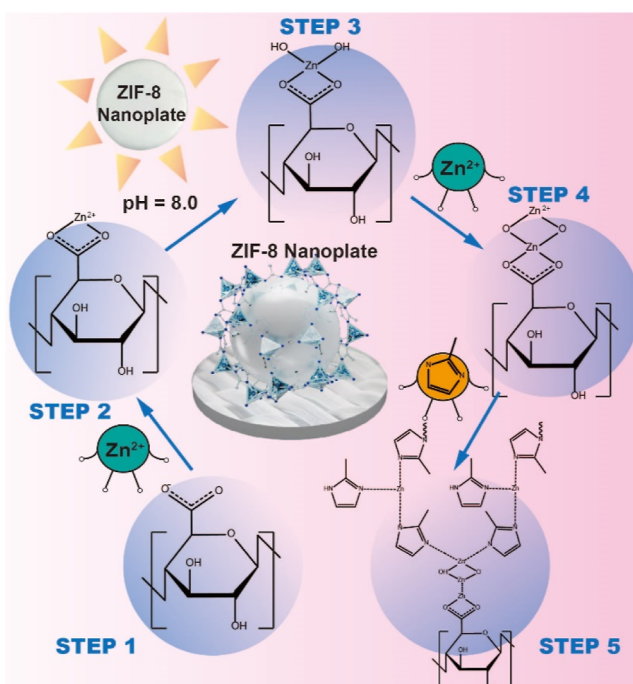


Figure 1. Fabrication process of the in situ ZIF-8 nanoplate.

dispersed in distilled water to a final content of 0.1 wt %, and the suspension was stirred sufficiently. (ii) 3.0 g of Zn(NO₃)₂·6H₂O was added to the above suspension until fully mixed. Zn(NO₃)₂ was thoroughly mixed with the suspension, facilitating efficient absorption of Zn ions onto the nanopaper surface through the electrostatic interaction with carboxyl groups. (iii) 8 mL of NaOH solution (4 mg/mL) was gradually dropped to the mixed suspension. The mixture was stirred at 1000 rpm for 2 h and stewed for another 1 h for adequate adsorption. The pH of the suspension was adjusted to approximately 8.0, followed by complete stirring and incubation in an alkaline solution to ensure sufficient Zn ion adsorption. This process resulted in the formation of an intermediate layer consisting of Zn(OH)₂, where excess Zn ions were linked to hydroxyl groups. (iv) The prepared suspension was vacuum-filtered on a glass filter holder with a PVDF filter membrane (VVLPO4700, EMD Millipore

Corporation, pore size: $0.1\text{ }\mu\text{m}$). Then, 50 mL of methanol was used for washing the filtered nanopaper “gel,” and this step was repeated for three times. (v) To form the *in situ* ZIF-8 nanoplate, the filtered gel paper was soaked in a 50 mg/mL 1,2-dimethylimidazole/methanol solution, and the upper layer shape was replicated to develop and anchor the ZIF-8 nanocrystals. The prepared film was fully washed and dried in oven for further application. The resulting *in situ* ZIF-8 nanoplates were prepared for subsequent SERS detection. When constructing layered composite materials or heterostructures, chemical transfer controls the interactions, diffusion, and possible reactions of different components at the interface, affecting the final structure and properties of the nanopaper-based composite material.^{20–22}

Preparation of Multiple SERS Detection MOF-PADs.

4.0 g of TEMPO-oxidized NFC slurry was dispersed in distilled water to a final content of 0.1 wt %, and the suspension was stirred sufficiently. Because ZIF-67 and ZIF-8 have the same organic ligands and *in situ* growth methods, they have been proven to have better SERS enhancement performance compared to other MOF materials. So, we chose to grow these two MOF materials *in situ* on nanopaper. A total of 3.0 g $\text{Co}(\text{NO}_3)_2 \cdot 6\text{H}_2\text{O}$ and $\text{Zn}(\text{NO}_3)_2 \cdot 6\text{H}_2\text{O}$, in different ratios, was added to the above suspension until fully mixed. The pH of the above suspension was adjusted to 8.0 with saturated NaOH solution. The mixture was stirred at 1000 rpm for 2 h and stewed for another 1 h for adequate adsorption. This process resulted in the formation of an intermediate layer consisting of $\text{Co}(\text{OH})_2$ and $\text{Zn}(\text{OH})_2$, respectively. The prepared suspension was vacuum-filtered on a glass filter holder with a PVDF filter membrane. Then, 50 mL of methanol per time was used for washing the filter gel three times. Next, the filtered nanopaper gel was soaked in 2 g/mL 1,2-dimethylimidazole/methanol solution for 12 h. The prepared film was fully washed with methanol for 0.5 h and dried in an oven for further application. The chemical formula of MOF-PADs is shown in Figure 2a.

Raman Measurement. Raman spectra were measured by a Renishaw Micro-Raman Spectroscopy System (London, U.K.) with 532 and 633 nm lasers with a $50\times$ objective, respectively. MO was dissolved in ethanol at concentrations ranging from 10^{-4} to 10^{-8} M. 5 μL of the analyte solution was dropped on the ZIF-8 nanoplate and further dried in air. The Raman spectra were recorded in the region of 600 to 1800 cm^{-1} under 633 nm. Moreover, 10⁻⁴ M MO was selected for optimization. For multiple Raman detection of the MOF-PADs, 10⁻⁷ M R6G and MO solution were tested under 532 and 633 nm, respectively. 5 μL of the R6G solution was dropped onto the MOF-PADs and allowed to dry in air. The Raman spectrum was acquired in the region of 600 to 1800 cm^{-1} under 532 nm. Then, the laser was changed to 633 nm, to detect MO analytes on MOF-PADs in the region of 600 to 1800 cm^{-1} under a 633 nm laser. Raman spectra were obtained as the average of five measurements. All spectral data were analyzed using the OriginLab software (OriginLab, U.S.A.).

Photoelectrochemical Measurements. By using an electrochemical workstation (Metrohm PGSTAT302N, Switzerland) in a handmade standard three-electrode cell, photo-electron chemistry experiments were tested. The saturated calomel electrode, Pt electrode, and FTO ($1 \times 1 \text{ cm}^2$) drop-coating homogeneous catalyst were utilized as the reference electrode, counter electrode, and working electrode, in that order. The Na_2SO_4 aqueous solution (0.5 M) served as the

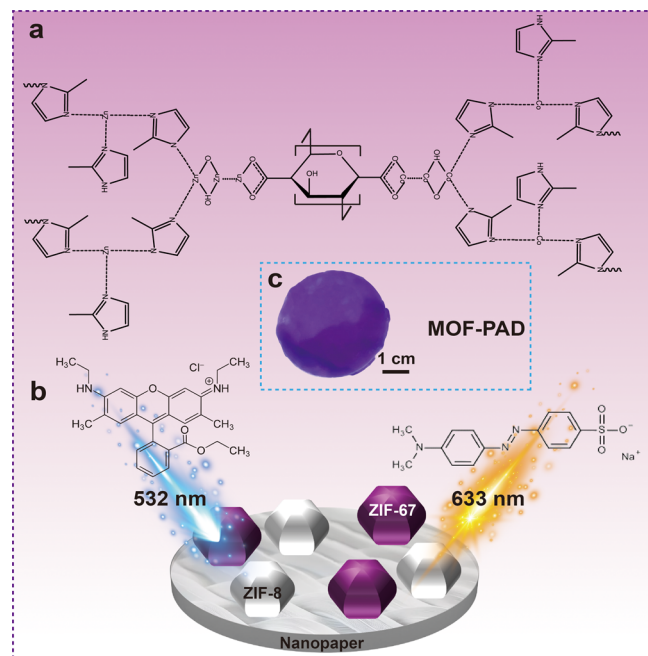


Figure 2. Structure and multiple SERS detection of MOF-PADs. (a) Structure of MOF-PADs. (b) Multiple SERS detection on MOF-PADs. (c) Photo of MOF-PADs.

electrolyte. The test bias of the photocurrent current density–time curve was 0 V under 1000 Hz. The voltage sweep range for the linear scanning voltammetry test was −1.0 to 1.0 V.

Instrumentation. Transmission electron microscopy (TEM) images were achieved with TEM at 50 kV accelerating voltage (FEI Talos F200X G2, U.S.A). Scanning electron microscopy (SEM) (FEI Scios 2 HiVac, U.S.A) was used to characterize the morphology of *in situ* ZIF-8 nanoplate and MOF-PADs at a working voltage of 5 kV. Energy-dispersive X-ray spectroscopic (EDS) analysis was performed to analyze elemental composition (FEI Scios 2 HiVac, U.S.A). X-ray photoelectron spectroscopy (XPS) (Thermo Scientific K-Alpha, U.S.A) was chosen to calculate element content and valence at a working voltage of 12 kV. The crystal phase was characterized by diffraction of X-rays (D8 ADVANCE, USA). OriginLab software (OriginLab, U.S.A) was used to analyze all data. Inductively coupled plasma optical emission spectroscopy was used to detect the loading rates of ZIF-67 and ZIF-8. By comparing the metal content in the filtrate and the original solution, the loading rates of the two were found to be 24 and 23%, respectively.

RESULTS

Characterization of the In Situ ZIF-8 Nanoplate. Several characterizations were carried out to confirm the successful generation of the ZIF-8/Zn(OH)₂ n–n junction structure on nanopaper. TEM images were employed to display structures. Figure 3a shows the equivalent TEM image of the artificial ZIF-8/Zn(OH)₂ nanostructure. It should be noted that the composite in Figure 3a shows the obvious lattice fringes with the interplanar spacings of 0.16 nm, which is in good agreement with the (0001) plane.²³ The ZIF-8/Zn(OH)₂ n–n junctions were successfully produced, and the clear lattice fringes show high crystallinity of the catalysts after calcination, according to the above analysis presented.

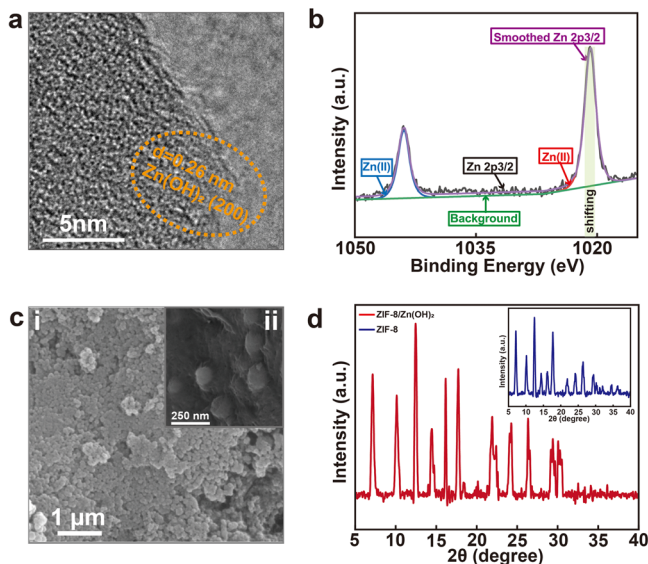


Figure 3. Characterization of the in situ ZIF-8 nanoplate. (a) TEM image of ZIF-8/Zn(OH)₂ n–n junction nanostructures. (b) XPS spectra of central metal Zn in the in situ ZIF-8 nanoplate. (c) SEM image of the in situ ZIF-8 nanoplate with (i) and without (ii) Zn(OH)₂. (d) XRD spectra of the in situ ZIF-8 nanoplate and pure ZIF-8 on nanopaper.

XPS was used to determine the valence state of Zn ions in the in situ ZIF-8 nanoplate. The XPS spectrum of each element in the in situ ZIF-8 nanoplate is displayed in Figure S1. Two signals that are compatible with the ligand's C and N atoms are observed in the C 1s and N 1s regions with energies of 285 and 401 eV, respectively.²⁴ Figure 3c shows the XPS spectra of Zn 2p, which has two peaks at 1043 and 1021 eV. The Zn(II) peak shifted from the expected 1019 to 1021 eV, demonstrating the electron transport from Zn(OH)₂ to ZIF-8 and supplying additional proof of the successful n–n junction construction.

By measuring the related X-ray diffraction (XRD) spectra, it was possible to verify the successful generation of ZIF-8/Zn(OH)₂ nanostructure. Figure 3d(i) illustrates the XRD patterns with 5 distinctive diffraction peaks located at 7.1, 10.1, 12.4, 16.2, and 17.7° crystals.²⁶ Peak broadening can be clearly observed from the sample XRD pattern, indicating the formation of nanosized crystals. This outcome shows that ZIF-8 with the upper layer crystal structure was successfully manufactured. The nanopaper is densely packed with in situ pure ZIF-8, confirming the material's exceptional purity. For comparison, Figure 3d(ii) shows the XRD pattern of a pure ZIF-8 crystal on nanopaper. The diffraction peaks of new crystalline materials, however, differ from those of the ZIF-8 crystal with the Zn(OH)₂ heterojunction but without significant change, indicating that the samples' framework structures were mostly preserved.

The SEM images of nanopaper with in situ ZIF-8 particles with and without Zn(OH)₂ are shown in Figure 3c(j,ii), respectively, which demonstrate average particle diameters of about 50 and 130 nm. There are only a few agglomerated particles, which suggests that the typical in situ ZIF-8 particles are not very effective. The dispersion of in situ ZIF-8 particles with the Zn(OH)₂ seems to be more even and continuous. In addition, the aforementioned figures demonstrate that the nanostructures structurally change from mesoporous to

microporous. As previously noted, a narrower pore size distribution reduces adsorbent obstruction and has a less significant effect on the adsorption of trace analytes.

The ZIF-8/Zn(OH)₂ n–n junction nanoplate shows a deeper hue compared with pure in situ ZIF-8 nanopaper, as illustrated in Figure S2a,b, respectively, where the reaction mechanism and color change can be easily observed with the naked eye. Due to its structural composition of tetrahedral ZnN₄ building blocks with cobalt ion centers coordinated by nitrogen atoms in imidazole linkers (Figure 1), ZIF-8 has an isoreticular structure. The carboxyl groups of the nanopaper bind to Zn ions, forming a layer of Zn(OH)₂ and hydroxyl bridges with residual Zn ions, which produces ZIF-8 in the upper layer. Collectively, the aforementioned characterizations show that the innovative ZIF-8/Zn(OH)₂ n–n junction structure on nanopaper, which may be used for SERS detection, was successfully developed.²⁷

Raman Enhancement Mechanisms. Semiconductor SERS substrates have been proven to show Raman enhancement via the chemical mechanism, whereas the electromagnetic mechanism is realized only on semiconductor substrates in longer wavelength regions (infrared wavelength).²⁸ While the p–n junction exhibits CT between the incident light and heterojunction, contributing efficient PICT to MOFs, the transferred electrons attract SERS enhancement.^{29–31} To further elucidate the role of the junction in the PICT process, the energy level schematic of the ZIF-8/Zn(OH)₂ molecule system is shown in Figure 4a. MO, a

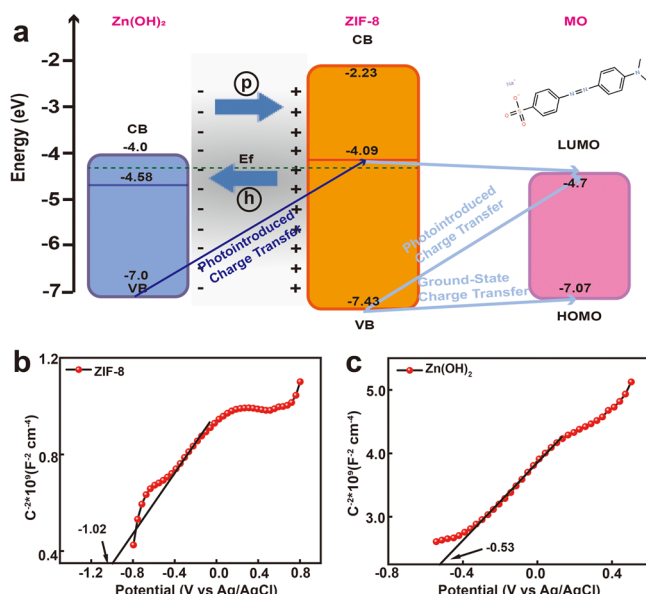


Figure 4. SERS mechanisms of a ZIF-8 nanoplate. (a) Energy level diagram of the MO molecule on a ZIF-8 nanoplate under the illumination of 633 nm. (b,c) Mott–Schottky analysis of ZIF-8 and Co(OH)₂, respectively.

common synthetic dye, is a pollutant that needs to be controlled due to its potential release into the environment, especially in water systems. Therefore, low-cost and high-sensitivity detection of MO is particularly important. ZIF-8 could be selected as an active substrate for MO detection, with HOMO and LUMO levels at -7.43 and -2.23 eV, respectively (Figure 4a). In this system, the CT from ZIF-8 to MO (2.73 eV) could be manipulated to approach the energy of the

incident laser (633 nm, 1.96 eV). Enhancement of SERS signals can also be attributed to ground-state charge-transfer (GSCT), which describes the CT between the aligned energy levels of the SERS substrate and analyte, even in the ground state. This phenomenon increases the polarizability of the analyte molecules. In the ZIF-8/MO system, GSCT may occur because ZIF-8's HOMO level (-7.43 eV) is close to MO's (-7.07 eV). Consequently, after coupling of such resonant transitions, the observed selectivity in SERS detection of distinct analytes on different MOFs would be explained by band-level alignment based on the wide range of band structures in MOFs. For MO systems, the characteristic vibrational bands of MO always exhibit stronger SERS signals at excitation wavelengths of 532 and 633 nm. However, ZIF-67 exhibits weak or no enhancement on MO at 633 nm. Therefore, an excitation wavelength of 633 nm was chosen to demonstrate the specificity of the ZIF-8 substrate for MO detection.

For the $\text{Zn}(\text{OH})_2$ –MO system, the excitation energy is insufficient to carry out CT from the HOMO of MO (-7.07 eV) to the valence band (VB) of $\text{Zn}(\text{OH})_2$ (-4.0 eV) or from the valence band (VB) of $\text{Zn}(\text{OH})_2$ (-7.0 eV) to the LUMO of MO (-4.70 eV).^{35,36} The polarization tensor was calculated using the formula $a + b + c$. According to theory, the Albrecht b or c terms serve as vibronic coupling term, through which the SERS induced by the CT effect might borrow intensity.^{32,33} However, b and c terms cannot be realized in the $\text{Zn}(\text{OH})_2$ –MO system.³⁴ These CT resonances significantly increase the polarization tensor of the probe, amplify the Raman scattering cross section, and contribute to the substantial overall Raman enhancement at 633 nm excitation. Also, under such conditions, the narrower pore size distribution supported by hydroxide reduces adsorbent obstruction and has a less significant effect on the adsorption of trace analytes, thereby further increase the SERS sensitivity.

Mott–Schottky plots were used to study the electron transport behavior of the synthesized polyhedron catalysts in the 0.5 M Na_2SO_4 electrolyte at a frequency of 1000 Hz. Figure 4b,c shows the spectra of ZIF-8 and $\text{Zn}(\text{OH})_2$, respectively. As displayed in Figure 4b,c, both ZIF-8 and $\text{Zn}(\text{OH})_2$ are negative slopes in the E – C^{2-} plots, respectively, indicating their n-type semiconductor characteristics. ZIF-8 and $\text{Zn}(\text{OH})_2$ trap electrons and holes near the interface at the n–n junction, respectively.³⁷ The horizontal intercept of the Mott–Schottky spectra indicates the Fermi level potential. Otherwise, the flat-band potential (E_{fb}) of the resulting ZIF-8 and $\text{Zn}(\text{OH})_2$ polyhedron are about -1.02 and -0.53 V (vs Ag/AgCl electrode), as shown in Figure 4b,c.³⁸ The flat band potential V_{fb} (vs Ag/AgCl) should transfer to the standard hydrogen electrode (SHE) by the following formula 1

$$E_{\text{SHE}} = E_{\text{Ag}/\text{AgCl}} + 0.197 \text{ V} + 0.0591 \times \text{pH} \quad (1)$$

The pH value of the aqueous Na_2SO_4 electrolyte was 7.0. Therefore, the V_{fb} values of ZIF-8 and $\text{Zn}(\text{OH})_2$ were estimated to be -0.41 and 0.08 V (vs SHE), respectively. In addition, the absolute potential value of SHE is -4.5 V. E_F relative formula 2 to the vacuum degree can be calculated as follows

$$E_F = e[-4.5 - E_{\text{SHE}}]V \quad (2)$$

Therefore, the E_F values were calculated to be -4.09 and -4.58 eV, respectively. Free electrons in the conduction band of ZIF-8 migrate to the conduction band of $\text{Zn}(\text{OH})_2$ until the

Fermi levels reach equilibrium. This process leads to the formation of an electron depletion layer in ZIF-8 and an electron accumulation layer in $\text{Zn}(\text{OH})_2$ at the interface. Finally, the Fermi energy levels of these two materials are equal, and provide more electrons transferring to analytes for SERS signal enhancing.³⁹ In other words, the presence of n–n junction provides more free electrons, which can provide stronger signals under laser excitation.^{9,34,40} When illuminated at 633 nm, these CT resonances significantly enhance the probe's polarization tensor, increase the Raman scattering cross-section, and contribute to the overall improvement of Raman signals in the heterojunction substrates.

SERS Detection Results of the In Situ ZIF-8 Nanoplate. Effective heterojunction production has a significant impact on SERS enhancement. In order to optimize the SERS sensitivity, we adjusted the pH of the suspension to control the amount of generated $\text{Zn}(\text{OH})_2$. 4, 6, 8, and 10 mL of a 4 mg/mL NaOH solution were added, corresponding to pH values of 6.0, 7.0, 8.0, and 9.0, respectively. As a sensing example, we verified the verification using the typical environmental contaminant MO (10^{-4} M in ethanol). Figure 5d illustrates

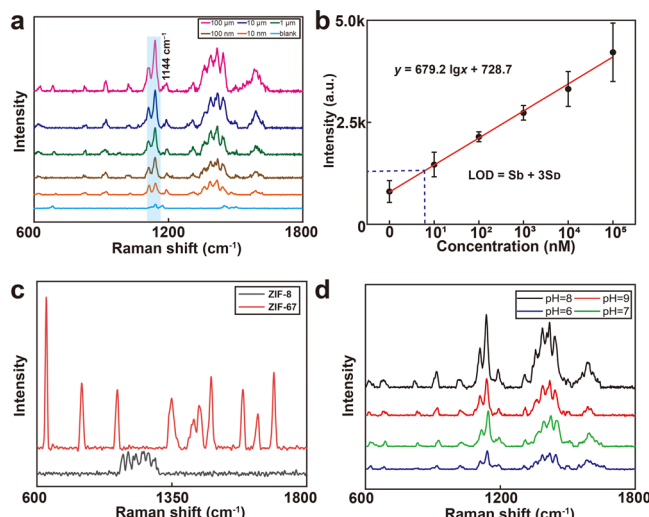


Figure 5. SERS-based detection of the in situ ZIF-8 Nanoplate (a) Raman spectra of MO at concentrations of 10 nM to 100 μM . (b) Calibration of MO at 1144 cm^{-1} ($n = 5$). (c) Comparison of R6G detection on in situ ZIF-8 and ZIF-67 nanoplates, respectively. (d) Optimization of in situ ZIF-8 nanoplates.

the Raman spectra of MO on ZIF-8 nanoplate under different pH values, where the distinctive peak of MO at 1144 cm^{-1} is most intense at pH = 8.0. Excessive hydroxyl introduction can cause all Zn ions to precipitate $\text{Zn}(\text{OH})_2$. In contrast, a trace of hydroxyl fails to generate enough $\text{Zn}(\text{OH})_2$, so the CT system cannot be generated, which restricts feasible CT between the heterojunction and ZIF-8. Because this indicates a mixture of both ZIF-8 and $\text{Zn}(\text{OH})_2$ rather than a single component, the binding energy approaching the center of ZIF-8 and $\text{Zn}(\text{OH})_2$ can produce stronger SERS signals. Therefore, we selected 8 mL of 4 mg/mL NaOH solution to adjust the pH value for further experiments.

MO, a prevalent environmental pollutant and low-toxicity organic chemical, was chosen as the sensing example to demonstrate the practical application of ZIF-8 nanoplates. The MO molecules were directly mixed with ethanol and the Raman spectra of MO samples at various concentrations in

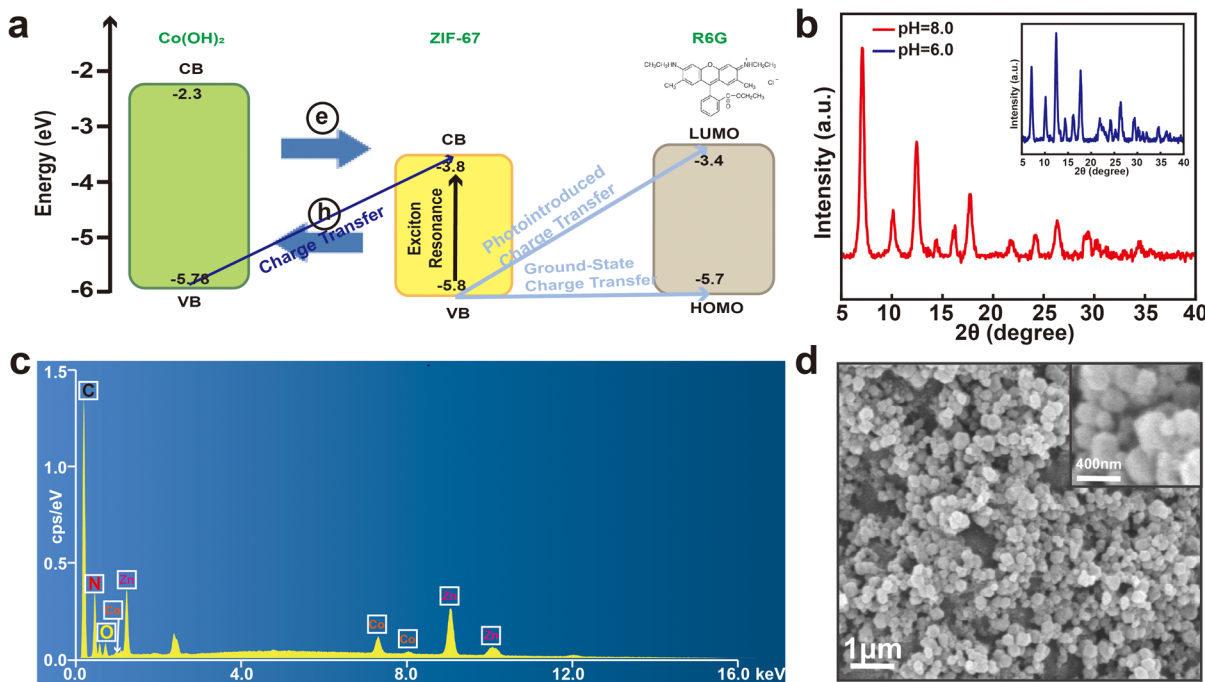


Figure 6. Characterization of MOF-PADs. (a) Energy level diagram of the R6G molecule on MOF-PADs under the illumination of 523 nm. (b) XRD spectra of both ZIF-67 and ZIF-8 lattices.⁴³ (c) EDS spectra of MOF-PADs. (d) SEM image of nanoparticles on MOF-PADs.

ethanol (10^{-4} to 10^{-8} M) are shown in Figure 5a, with pure ethanol serving as the blank control. The spectra exhibited strong MO bands, including S–O– stretch (1113 cm^{-1}), N–N bend (1144 cm^{-1}), C–N bend (1350 cm^{-1}), (C–) SO₂ (–O) stretch (1397 cm^{-1}), C–N torsion (1445 cm^{-1}), and N–H stretch (1590 cm^{-1}). At an ultralow concentration of 10^{-8} M, the fingerprint Raman bands remained detectable. This remarkable LOD highlights the potential of ZIF-8 nanoplate as an ultrasensitive platform. Since the intensity of the 1144 cm^{-1} band is more sensitive to MO concentration with minimal background noise, this peak was selected for quantitative analysis. The calibration curve of MO detection is shown in Figure 5b, with a calculated LOD of 4.44 nM , defined as the MO concentration corresponding to the blank control intensity plus three times the standard deviation of the Raman intensity of the blank. The linear regression equation was $y = 679.2 \lg x + 728.7$, with a correlation coefficient (R^2) of 0.99 ($n = 5$). The system exhibited a well-defined linear response to molecular concentration. The ZIF-8 nanoplate LOD attained for MO is several times improved over the previous one.

In order to assess the SERS activity of the ZIF-8 nanoplate, the EF was calculated using the equation $\text{EF} = \frac{I_{\text{SERS}}}{I_{\text{bare}}} \times \frac{C_{\text{bare}}}{C_{\text{SERS}}}$, where I_{SERS} and C_{SERS} are the intensities of the Raman spectra of MO at 1144 cm^{-1} with the SERS effect and concentrations on ZIF-8 nanopaper, and I_{bare} and C_{bare} are on bare nanopaper. Its strong SERS sensitivity to MO was confirmed by the computed EF for the ZIF-8 plate, found to be 3.07×10^5 , which is similar as other MOFs-based SERS substrates. This value is similar to the performance of contemporary inorganic semiconductors and precious metals. ZIF-8 nanoplates can significantly improve the SERS sensitivity and can be further applied in other applications. The stability of ZIF-8 nanoplate stored at room temperature for several weeks is shown in Figure S3. Although a slight decrease in the peak value was

observed with increasing storage time, there is no change in the peak value of the low peak. However, increasing the storage time of the ZIF-8 nanoplate did not increase the noise of SERS detection. This confirms the reliability of our preparation method.

To demonstrate how structural flexibility affects the SERS performance of MOFs more clearly, R6G was chosen as a demonstration. When R6G was employed as the target molecule, its HOMO and LUMO levels were -5.70 and -3.40 eV , respectively. The HOMO of the ZIF-67 was -5.80 eV , and HOMO-to-LUMO CT transitions between ZIF-67 and R6G may exist in ZIF-67 under 633 nm laser excitation. However, the VB and CB levels of ZIF-8 were -7.43 eV and -2.23 eV , which cannot contribute to the PICT between the ZIF-8's VB to the HOMO of R6G. The ZIF-8 nanoplates we developed retained the selectivity of the MOF substrate.

Characterization of MOF-PADs. The tailorability and selectivity of MOFs make them attractive SERS-enhancing materials; however, this ability also restricts the SERS detection for multiple molecule analytes. Because the CT mechanism between MOFs and analytes, only one type of MOF can determine objects in a specific area of HUMO and LUMO. To solve this limitation and still reserve the selection of MOFs, we developed MOF-PADs generated with both in situ ZIF-8/Zn(OH)₂ and ZIF-67/Co(OH)₂, by shifting the incident laser length from 633 to 532 nm for initiating PICT between ZIF-8 to MO and ZIF-67 to R6G, respectively. The MOF-PADs we fabricated maintained independent CT processes for different MOFs/M_x(OH)_y systems. The fabrication process of multiple Raman detection MOF-PADs was similar to that for in situ ZIF-8 nanoplates. Both Co(NO₃)₂·6H₂O and Zn(NO₃)₂·6H₂O were mixed with nanocellulose, and the pH of the above suspension was adjusted to 8.0 – 8.5 . Within this pH range, both Zn and Co ions could fully bind with excess imidazole ligands, avoiding preferential or excessive deposition of one ion.^{41,42} Zn and Co

ions facilitated efficient absorption onto the nanopaper surface through electrostatic interaction with carboxyl groups randomly. Figure 2b shows a photo of MOF-PADs. Instead of the complicated fabrication of different MOFs independently, the MOF-PADs we provided enable straightforward and effective SERS detection of various molecules.

Additional investigations were conducted to provide a more thorough description of the underlying SERS mechanisms on MOF-PADs. The R6G probe's HOMO and LUMO values are -5.70 eV and -3.40 eV , respectively. Electrons in the VB of ZIF-67 (-5.80 eV) are injected into the LUMO of R6G molecules (-3.40 eV). The electron absorption threshold for R6G is approximately $555\text{--}579\text{ nm}$, and the ZIF-67/ Co(OH)_2 -R6G complex red-shifts the absorption peak to about 532 nm , providing clear evidence for efficient CT between adsorbed molecules and ZIF-67/ Co(OH)_2 (37). The CT transition energy is close to the excitation laser energy of 532 nm ($\lambda = 2.33\text{ eV}$), resulting in particularly poor SERS enhancement. In contrast, the interface CT energy from ZIF-67 to R6G is 2.4 eV , which effectively resonates with the laser energy of 2.33 eV . Therefore, this explains why ZIF-67 has relatively high SERS activity as a substrate in R6G detection. The molecular transition between the HOMO and LUMO levels of R6G at 2.3 eV is also close in energy to the molecular transition of the excited laser, providing another resonant pathway for further enhancing the SERS effect. However, ZIF-8 cannot achieve energy transition to R6G at excitation wavelengths of 532 and 633 nm . Therefore, in this case, we chose 532 nm as the excitation wavelength for R6G detection. The energy level diagram of ZIF-67/ Co(OH)_2 p-n junction under illumination at 532 nm is shown in Figure 6a. The VB of ZIF-8 (-2.33 eV) is much higher than R6G's LUMO, so electron CT occurs from ZIF-8's VB to CB rather than from ZIF-8's VB to R6G's LUMO, which indicated that SERS detection of R6G does not happen. Furthermore, in the SERS detection of MO with ZIF-8, the GSCT transition is more important, as it increases the polarizability of the analyte molecules. The GSCT from ZIF-8 to MO reflects the CT between the aligned energy levels of the SERS substrate and the analyte, even in the ground state. The ZIF-8/ Zn(OH)_2 -MO system shows the best SERS result when excited by 633 nm instead of 532 nm , due to the different excitation wavelength matching conditions. In the ZIF-8/ Zn(OH)_2 -MO system, GSCT may be anticipated since ZIF-8's VB level is close to MO's HOMO (-7.07 eV) at -7.43 eV .

Several characterizations were carried out to confirm the successful formation of the ZIF-67 and ZIF-8 crystals on nanopaper. By measuring the related XRD spectra, it was possible to verify that ZIF-67 and ZIF-8 crystals had been successfully generated. Figure 6b illustrates the XRD patterns with distinctive diffraction peaks located at 7.1 , 10.1 , 12.5 , 16.2 , and 17.8° crystals.⁴³ Peak broadening can be clearly observed from the sample XRD pattern, indicating the formation of those two nanosized crystals. This outcome shows that ZIF-67 and ZIF-8 with upper layer crystal structures were successfully manufactured. The XPS spectrum of each element on MOF-PAD is also displayed in Figure S7, while the peaks of Zn and Co are around $1051.98\text{--}1021.3\text{ eV}$ and $811.98\text{--}780.56\text{ eV}$, respectively. This spectrum illustrates the successful generation of ZIF-67 and ZIF-8 systems.

The SEM images of MOF-PADs containing both in situ ZIF-67 and ZIF-8 particles are shown in Figure 6d. The dispersion of these nanoparticles seems to be generated evenly

and continuously on nanopaper. As previously mentioned, a narrower pore size distribution reduces adsorbent obstruction and has a less significant effect on the adsorption of trace analytes. A TEM image of MOF-PADs is shown in Figure S6, further confirming the successful generation of this platform. To confirm the presence of MOF-PADs, the chemical compositions of pristine ZIF-67 and ZIF-8 were further determined, as shown in Figure 6c. While pristine ZIF-67 exhibited significant peaks corresponding to Co, N, and C, the pristine ZIF-8 exhibited those of Zn, N, and C. Moreover, a notable peak of O and H was observed, suggesting that the MOF-PADs might contain hydroxide, possibly due to the presence of metal hydroxides. The element distribution maps and contents are shown in Figure S5 and Table S2. The contents of Zn and Co elements are nearly the same under the same quantity of Co and Zn ions, which indicates that no metal ion has undergone transition bonding. The characterization above shows the successful generation of both ZIF-67 and ZIF-8 on nanopaper. To verify the stability of MOF-PADs under extreme conditions, we soaked them in strong acid ($\text{pH} = 0.0$) and strong alkali ($\text{pH} = 14.0$) conditions for 5 min. The SEM images are shown in Figure S9, where the MOF particles soaked in a strong alkaline environment did not show significant changes, because the imidazole group is relatively stable under alkaline conditions. Strong acid can cause the metal ligand coordination bond to break and the framework structure to collapse, and nanocellulose will be hydrolyzed by acid. Therefore, MOF particles underwent slight agglomeration (Figure S9a), suggesting that prolonged exposure to strong acids could lead to functional loss of the platform. The mechanical strength of MOF-PADs is also an important parameter. The average value of its elastic modulus is 438.66 MPa ($n = 3$), as shown in Table S3, indicating that our MOF-PADs have good mechanical properties that can meet the needs of practical detection.

Multiple SERS Detection on MOF-PADs. MOF-PADs were used to detect different molecules by utilizing the ZIF-67 and ZIF-8 on them, respectively. Figure 7a illustrates the

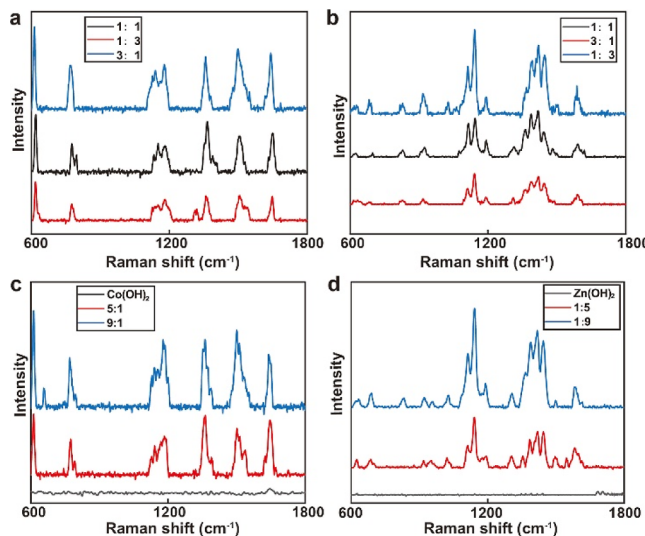


Figure 7. SERS detection results on MOF-PADs. (a,c) Raman spectra of R6G at a concentration of 100 nM under different MOF-PADs. (b,d) Raman spectra of MO at a concentration of 100 nM under different MOF-PADs. (The ratio was defined as the quantity of $\text{Co}^{2+}/\text{Zn}^{2+}$ added for fabricating MOF-PADs.).

Raman spectra of R6G (10^{-7} M) on MOF-PADs under a 532 nm laser with different concentrations of Co and Zn ions, indicating different quantities of ZIF-67 and ZIF-8 on the same nanopaper. The figure shows the Raman spectra of R6G samples in ethanol, revealing peaks at, including C–C ring bending (610 cm^{-1}), C–H out bending (774 cm^{-1}), C–H in bending (935 cm^{-1}), C–O–C stretching (1184 cm^{-1} and 1282 cm^{-1}), and aromatic C–C stretching (1310 cm^{-1} , 1364 cm^{-1} , 1508 cm^{-1} , 1578 cm^{-1} , and 1648 cm^{-1}). With the decrease of Co ions, the intensity of R6G also decreases. Then, the incident light was changed to 633 nm, and the detection of MO was realized with the corresponding characteristic peaks. Similar to R6G, with the increase of Zn ions, more ZIF-8 was generated on MOF-PADs, and the Raman intensity of MO increases. Both 10^{-7} M MO and R6G can be detected on these MOF-PADs under this ratio of Zn and Co ions. For the optimization of the MOF-PADs performance, the ratio of the quantity of Co/Zn content ranged from 1:9 to 9:1 (the quantity of $\text{Co}(\text{NO}_3)_2$ and $\text{Zn}(\text{NO}_3)_2$ is 3.0 g in total for fabricating MOF-PADs with different Co and Zn ion ratios). From Figure 7c, it can be seen that the excessive Zn ions limit the generation of ZIF-67, while the MOF-PADs can only detect the MO under 633 nm ($\text{Zn}/\text{Co} \geq 5:1$). In contrast, excessive Co ions occupied the majority of carboxyl groups, so the generation of ZIF-8 was restricted ($\text{Co}/\text{Zn} \geq 5:1$), as shown in Figure 7d. It is observed from those two figures that the multiple SERS detection can only be realized between the ratio of Co and Zn ions among 3:1 to 1:3. With the increase of the introduction of ZIF-67, the intensity of R6G rose and the results of MO dropped at the same concentration. Similarly, the increased content of ZIF-8 contributes to the growth of MO's intensity and the decrease of R6G. Compared with the lowest concentration that can be detected in pure ZIF-8 and ZIF-67 achieved in the previous work (10^{-7} M), the LOD of MOF-PADs we designed was similar, indicating that the LOD of MOF-PADs was not sacrificed. Although these MOF-PADs cannot achieve the same high sensitivity as before, MOF-PADs can still satisfy the detection in wide applications and be extended to more areas, while still retaining their tailorability. Moreover, the high optical transparency of MOF-PADs reduces signal loss by light reflection, which also contributes to the high SERS performance. These observations provide a new strategy for the promising future of the design of efficient CT substrates.

The CT from ZIF-8 to MO (2.73 eV) could be manipulated to better match the energy of the incident laser (633 nm, 1.96 eV), when compared with that of ZIF-67 (1.1 eV), so we use ZIF-8 to detect MO under a 633 nm laser. Also, the transfer from ZIF-67 to R6G is close to the energy of a 532 nm laser. MOF-PADs also showed better stability when stored at room temperature. We selected the test substance with a concentration of 10^{-4} M for detection. For the ZIF-67 system, MOF-PADs stored for different times did not show significant attenuation in the detection intensity of R6G, but the platform stored for 2 weeks showed relatively better results. For the ZIF-8 system, the signal of MO showed attenuation and increased noise after being stored for 1 month. This may be due to the weaker wavelength energy of 633 nm, which requires higher stability of the ZIF-8. However, MOF-PADs as a whole exhibited excellent stability. Although MOF may bind with another metal oxide during the adsorption process, the excessive generation of MOF did not result in a significant decrease in sensitivity. So, the MOF-PADs are customizable

with other types of MOFs and expand the detection range, which may further promote the development of MOF-based applications.

CONCLUSION

In this study, we developed special ZIF-8/ $\text{Zn}(\text{OH})_2$ n–n junction structures to enhance SERS detection. The n–n junction not only generated near-field Raman enhancement but also facilitated CT. Consequently, the efficiency of PICT between the semiconducting substrate and the molecules was significantly enhanced through direct interfacial CT processes at the heterojunction. With the combined contributions of direct interfacial CT and plasmon-induced CT, the efficiency of PICT between the semiconducting substrate and molecules was greatly increased. For instance, using MO as the target molecule at an excitation wavelength of 633 nm, the SERS behaviors of in situ ZIF-8 nanoplates were examined, achieving a remarkable LOD of 4.44 nM . Moreover, to enable multiple molecules SERS detection while maintaining the selectivity of MOFs, we successfully generated MOF-PADs with both in situ ZIF-8/ $\text{Zn}(\text{OH})_2$ and ZIF-67/ $\text{Co}(\text{OH})_2$ systems. Two common environmental pollutants, MO and R6G, were selected as the sensing examples for proof. By using different incident light wavelengths, the PICT was realized independently among those two systems, and the LOD can be down to 10^{-7} M. Although the sensitivity of our platforms have not significantly improved compared to other MOFs-based SERS substrates, we ensure better stability and achieve more functionality. Our findings provide fresh opportunities for sensitive and focused detection in a range of contexts, including the search for adulteration in pharmaceuticals. The versatility and adaptability of MOFs offer tremendous potential for future developments in SERS-based sensing devices.

ASSOCIATED CONTENT

Supporting Information

The Supporting Information is available free of charge at <https://pubs.acs.org/doi/10.1021/acs.analchem.5c02659>.

XPS survey spectrum of the ZIF-8 nanoplate; photographs of in situ ZIF-8 nanoplates without (a) and with (b) $\text{Zn}(\text{OH})_2$ n–n junction; SERS spectra of MO on ZIF-8 nanoplate stored for different weeks; Specific SERS spectra of different concentrations of MO with R6G interference on ZIF-8 nanoplate; EDS elemental mapping of Zn, C, Co, O, and N; TEM image of MOF-PAD; XPS survey spectrum of the MOF-PADs; SERS spectra of R6G and MO on MOF-PADs stored for different weeks; SEM images of MOF-PADs; the coefficients of variation for SERS detection of MO at various concentrations; elemental composition of the sample determined by EDS; and mechanical properties of MOF-PADs ([PDF](#))

AUTHOR INFORMATION

Corresponding Authors

Fuzhou Niu – School of Mechanical Engineering, Suzhou University of Science and Technology, Suzhou 215009, China;  orcid.org/0000-0002-1847-4920; Email: fzniu@usts.edu.cn

Pengfei Song – School of Advanced Technology, Xi'an Jiaotong—Liverpool University, 215123 Suzhou, China; Department of Electrical Engineering and Electronics,

University of Liverpool, L69 7ZX Liverpool, U.K.;
ORCID.org/0000-0001-6337-7292; Email: pengfei.song@xjtu.edu.cn

Authors

Wenwen Yuan – School of Advanced Technology, Xi'an Jiaotong—Liverpool University, 215123 Suzhou, China; Department of Electrical Engineering and Electronics, University of Liverpool, L69 7ZX Liverpool, U.K.; College of Information Engineering, Shanghai Maritime University, 201306 Shanghai, China

Keran Jiao – School of Advanced Technology, Xi'an Jiaotong—Liverpool University, 215123 Suzhou, China

Ruiqi Yong – School of Advanced Technology, Xi'an Jiaotong—Liverpool University, 215123 Suzhou, China

Hang Yuan – School of Advanced Technology, Xi'an Jiaotong—Liverpool University, 215123 Suzhou, China

Shan Cong – Suzhou Institute of Nano-Tech and Nano-Bionics, Chinese Academy of Sciences, 215123 Suzhou, China; ORCID.org/0000-0002-5305-1237

Eng Gee Lim – School of Advanced Technology, Xi'an Jiaotong—Liverpool University, 215123 Suzhou, China; Department of Electrical Engineering and Electronics, University of Liverpool, L69 7ZX Liverpool, U.K.

Ivona Mitrović – Department of Electrical Engineering and Electronics, University of Liverpool, L69 7ZX Liverpool, U.K.

Jinyu Zhou – Suzhou Institute of Nano-Tech and Nano-Bionics, Chinese Academy of Sciences, 215123 Suzhou, China

Complete contact information is available at:

<https://pubs.acs.org/10.1021/acs.analchem.5c02659>

Author Contributions

All authors have given approval to the final version of the manuscript.

Notes

The authors declare no competing financial interest.

ACKNOWLEDGMENTS

The authors acknowledge the financial support from the programs of the Natural Science Foundation of the Jiangsu Higher Education (24KJB460030) and XJTLU RDF project (RDF-21-02-076). This work is also partially supported by the XJTLU AI University Research Centre, Jiangsu Province Engineering Research Centre of Data Science and Cognitive Computation at XJTLU, and the SIP AI innovation platform (YZCXPT2022103). This work also acknowledges Jiangsu Provincial Outstanding Youth Program (BK20230072), Suzhou Industrial Foresight and Key Core Technology Project (SYC2022044), and grants from Jiangsu QingLan Project and Jiangsu 333 high-level talents.

REFERENCES

- (1) Farha, O. K.; Özgür Yazaydin, A.; Eryazici, I.; Malliakas, C. D.; Hauser, B. G.; Kanatzidis, M. G.; Nguyen, S. T.; Snurr, R. Q.; Hupp, J. T. *Nature Chem.* **2010**, *2* (11), 944–948.
- (2) Furukawa, H.; Cordova, K. E.; O’Keeffe, M.; Yaghi, O. M. *Science* **2013**, *341* (6149), 1230444.
- (3) Li, J. F.; Huang, Y. F.; Ding, Y.; Yang, Z. L.; Li, S. B.; Zhou, X. S.; Fan, F. R.; Zhang, W.; Zhou, Z. Y.; Wu, D. Y.; Ren, B.; Wang, Z. L.; Tian, Z. Q. *Nature* **2010**, *464* (7287), 392–395.
- (4) Zhang, H.; Zhang, X.-G.; Wei, J.; Wang, C.; Chen, S.; Sun, H.-L.; Wang, Y.-H.; Chen, B.-H.; Yang, Z.-L.; Wu, D.-Y.; Li, J.-F.; Tian, Z. Q. *J. Am. Chem. Soc.* **2017**, *139* (30), 10339–10346.
- (5) Zhang, H.; Duan, S.; Radjenovic, P. M.; Tian, Z.-Q.; Li, J.-F. *Acc. Chem. Res.* **2020**, *53* (4), 729–739.
- (6) Pieczonka, N. P. W.; Aroca, R. F. *Chem. Soc. Rev.* **2008**, *37* (5), 946–954.
- (7) Nie, S.; Emory, S. R. *Science* **1997**, *275* (5303), 1102–1106.
- (8) Alessandri, I.; Lombardi, J. R. *Chem. Rev.* **2016**, *116* (24), 14921–14981.
- (9) Li, M.; Fan, X.; Gao, Y.; Qiu, T. *J. Phys. Chem. Lett.* **2019**, *10* (14), 4038–4044.
- (10) Cong, S.; Yuan, Y.; Chen, Z.; Hou, J.; Yang, M.; Su, Y.; Zhang, Y.; Li, L.; Li, Q.; Geng, F.; Zhao, Z. *Nat. Commun.* **2015**, *6* (1), 7800.
- (11) Lin, Z.-J.; Lü, J.; Hong, M.; Cao, R. *Chem. Soc. Rev.* **2014**, *43* (16), 5867–5895.
- (12) Kreno, L. E.; Leong, K.; Farha, O. K.; Allendorf, M.; Van Duyne, R. P.; Hupp, J. T. *Chem. Rev.* **2012**, *112* (2), 1105–1125.
- (13) Sun, H.; Cong, S.; Zheng, Z.; Wang, Z.; Chen, Z.; Zhao, Z. *J. Am. Chem. Soc.* **2019**, *141* (2), 870–878.
- (14) Sun, H.; Song, G.; Gong, W.; Lu, W.; Cong, S.; Zhao, Z. *Nano Res.* **2022**, *15* (6), 5347–5354.
- (15) Yuan, W.; Jiao, K.; Yuan, H.; Sun, H.; Lim, E. G.; Mitrović, I.; Duan, S.; Cong, S.; Yong, R.; Li, F.; Song, P. *ACS Appl. Mater. Interfaces* **2024**, *16* (20), 26374–26385.
- (16) Lai, H.; Shang, W.; Yun, Y.; Chen, D.; Wu, L.; Xu, F. *Microchim. Acta* **2019**, *186* (3), 144.
- (17) Yuan, W.; Yuan, H.; Jiao, K.; Zhu, J.; Lim, E. G.; Mitrović, I.; Duan, S.; Wang, Y.; Cong, S.; Zhao, C.; Sun, J.; Liu, X.; Song, P. *ACS Appl. Mater. Interfaces* **2023**, *15* (5), 6420–6430.
- (18) Yuan, W.; Yuan, H.; Duan, S.; Yong, R.; Zhu, J.; Lim, E. G.; Mitrović, I.; Song, P. *JoVE* **2023**, *200*, No. e65965.
- (19) Chen, L.; Ying, B.; Song, P.; Liu, X. *Adv. Mater. Interfaces* **2019**, *6* (24), 1901346.
- (20) Singh, J.; Rishikesh; Kumar, S.; Soni, R. K. *J. Alloys Compd.* **2020**, *849*, 1S6502.
- (21) Singh, J.; Soni, R. K.; Nguyen, D. D.; Kumar Gupta, V.; Nguyen-Tri, P. *Chemosphere* **2023**, *339*, 139735.
- (22) Singh, J.; Soni, R. K. *Colloids Surf., A* **2021**, *626*, 127005.
- (23) Zhu, L.; Li, H.; Liu, Z.; Xia, P.; Xie, Y.; Xiong, D. *J. Phys. Chem. C* **2018**, *122* (17), 9531–9539.
- (24) Liu, B.; Jian, M.; Wang, H.; Zhang, G.; Liu, R.; Zhang, X.; Qu, J. *Colloids Surf., A* **2018**, *538*, 164–172.
- (25) Tian, F.; Cerro, A. M.; Mosier, A. M.; Wayment-Steele, H. K.; Shine, R. S.; Park, A.; Webster, E. R.; Johnson, L. E.; Johal, M. S.; Benz, L. *J. Phys. Chem. C* **2014**, *118* (26), 14449–14456.
- (26) Pan, Y.; Liu, Y.; Zeng, G.; Zhao, L.; Lai, Z. *Chem. Commun.* **2011**, *47* (7), 2071–2073.
- (27) Cho, H.-Y.; Yang, D.-A.; Kim, J.; Jeong, S.-Y.; Ahn, W.-S. *Catal. Today* **2012**, *185* (1), 35–40.
- (28) Yamamoto, Y. S.; Itoh, T. *J. Raman Spectrosc.* **2016**, *47* (1), 78–88.
- (29) Hutter, E.; Fendler, J. H. *Adv. Mater.* **2004**, *16* (19), 1685–1706.
- (30) Fan, X.; Hao, Q.; Li, M.; Zhang, X.; Yang, X.; Mei, Y.; Qiu, T. *ACS Appl. Mater. Interfaces* **2020**, *12* (25), 28783–28791.
- (31) Fan, X.; Hao, Q.; Qiu, T.; Chu, P. K. *J. Appl. Phys.* **2020**, *127* (4), 040901.
- (32) Lombardi, J. R.; Birke, R. L. *Acc. Chem. Res.* **2009**, *42* (6), 734–742.
- (33) Yu, D.; Xu, L.; Zhang, H.; Li, J.; Wang, W.; Yang, L.; Jiang, X.; Zhao, B. *Chin. Chem. Lett.* **2023**, *34* (7), 107771.
- (34) Lombardi, J. R.; Birke, R. L. *J. Phys. Chem. C* **2014**, *118* (20), 11120–11130.
- (35) Emara, M. M.; Ragab, D. M.; Kassem, T. S. *J. Phys. Chem. Solids* **2021**, *148*, 109702.
- (36) Fageria, P.; Nazir, R.; Gangopadhyay, S.; Barshilia, H. C.; Pande, S. *RSC Adv.* **2015**, *5* (98), 80397–80409.
- (37) Xue, D.; Wang, J.; Wang, Y.; Sun, G.; Cao, J.; Bala, H.; Zhang, Z. *Nanomaterials* **2019**, *9* (3), 351.
- (38) Saliba, D.; Ammar, M.; Rammal, M.; Al-Ghoul, M.; Hmadeh, M. *J. Am. Chem. Soc.* **2018**, *140* (5), 1812–1823.

- (39) Li, G.; Zhang, X.; Lu, H.; Yan, C.; Chen, K.; Lu, H.; Gao, J.; Yang, Z.; Zhu, G.; Wang, C.; He, Z. *Sens. Actuators, B* **2019**, *283*, 602–612.
- (40) Jiang, X.; Xu, L.; Ji, W.; Wang, W.; Du, J.; Yang, L.; Song, W.; Han, X.; Zhao, B. *Appl. Surf. Sci.* **2022**, *584*, 152609.
- (41) Hu, S.; Yang, L.-L.; Yan, C.; Xiao, Y.; Jin, Z.; Gan, X.; Zhang, B.; Wu, W. *Chem. Eng. J.* **2024**, *498*, 154844.
- (42) Naderi, M.; Goharrizi, A. S.; Wu, H.; Barani, M.; Kamyabi, A. *Colloids Surf., A* **2025**, *718*, 136881.
- (43) Zhou, K.; Mousavi, B.; Luo, Z.; Phatanasri, S.; Chaemchuen, S.; Verpoort, F. *J. Mater. Chem. A* **2017**, *5* (3), 952–957.



CAS INSIGHTS™
EXPLORE THE INNOVATIONS SHAPING TOMORROW

Discover the latest scientific research and trends with CAS Insights. Subscribe for email updates on new articles, reports, and webinars at the intersection of science and innovation.

[Subscribe today](#)

CAS
A division of the
American Chemical Society